

Wave-Based Non-Line-of-Sight Imaging using Fast $f-k$ Migration

DAVID B. LINDELL, Stanford University

GORDON WETZSTEIN, Stanford University

MATTHEW O'TOOLE, Carnegie Mellon University

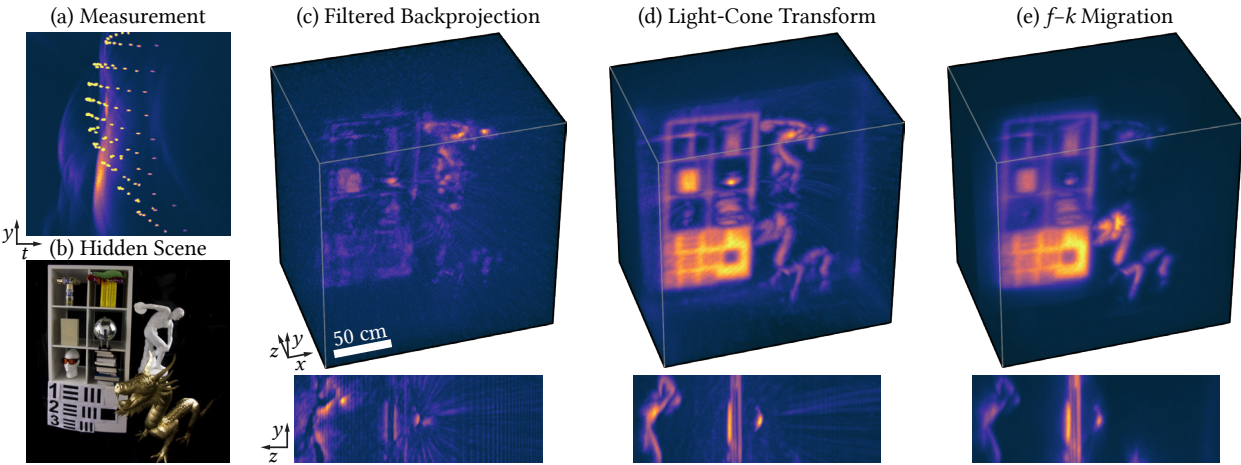


Fig. 1. Non-line-of-sight (NLOS) reconstructions of a hidden, room-sized scene. (a–b) One approach to NLOS imaging is to capture time-resolved measurements sampled across a visible surface, and reconstruct the 3D shape and reflectance of the hidden scene. A disco ball produces the bright dots seen in the measurements of indirect light transport (a), and other diffuse and glossy objects produce the streaks. (c) Among the various methods for reconstructing shape and reflectance from these measurements, filtered backprojection (FBP) is conceptually one of the simpler methods; it involves a delay-and-sum (backprojection) operation of the time-resolved measurements, followed by a heuristic high-pass filter on the result. (d) The light-cone transform (LCT) is a fast reconstruction algorithm that produces more accurate reconstructions in less time, but requires making restrictive assumptions on light transport (e.g., assumes the scene only contains diffuse objects). (e) In this paper, we introduce $f-k$ migration, an algorithm that is both fast and versatile, for NLOS imaging. The wave-based nature of this inverse method is unique in being robust to objects with diverse and complex reflectance properties, such as the glossy dragon, the diffuse statue, and the reflective disco ball shown in this scene. All volumes are rendered as maximum intensity projections.

Imaging objects outside a camera's direct line of sight has important applications in robotic vision, remote sensing, and many other domains. Time-of-flight-based non-line-of-sight (NLOS) imaging systems have recently demonstrated impressive results, but several challenges remain. Image formation and inversion models have been slow or limited by the types of hidden surfaces that can be imaged. Moreover, non-planar sampling surfaces and non-confocal scanning methods have not been supported by efficient NLOS algorithms. With this work, we introduce a wave-based image formation model for the problem of NLOS imaging. Inspired by inverse methods used in seismology, we adapt a frequency-domain method, $f-k$ migration, for solving the inverse NLOS problem. Unlike existing NLOS algorithms,

$f-k$ migration is both fast and memory efficient, it is robust to specular and other complex reflectance properties, and we show how it can be used with non-confocally scanned measurements as well as for non-planar sampling surfaces. $f-k$ migration is more robust to measurement noise than alternative methods, generally produces better quality reconstructions, and is easy to implement. We experimentally validate our algorithms with a new NLOS imaging system that records room-sized scenes outdoors under indirect sunlight, and scans persons wearing retroreflective clothing at interactive rates.

CCS Concepts: • Computing methodologies → 3D imaging; Computational photography.

Additional Key Words and Phrases: computational photography, time-of-flight imaging, non-line-of-sight imaging

ACM Reference Format:

David B. Lindell, Gordon Wetzstein, and Matthew O'Toole. 2019. Wave-Based Non-Line-of-Sight Imaging using Fast $f-k$ Migration. *ACM Trans. Graph.* 38, 4, Article 116 (July 2019), 13 pages. <https://doi.org/10.1145/3306346.3322937>

Authors' addresses: David B. Lindell, lindell@stanford.edu; Gordon Wetzstein, gordon.wetzstein@stanford.edu, Department of Electrical Engineering, Stanford University, Stanford CA, 94305, USA; Matthew O'Toole, mpotoole@cmu.edu, Robotics Institute & Computer Science Department, Carnegie Mellon University, Pittsburgh, Pennsylvania 15213, USA.

Permission to make digital or hard copies of all or part of this work for personal or classroom use is granted without fee provided that copies are not made or distributed for profit or commercial advantage and that copies bear this notice and the full citation on the first page. Copyrights for components of this work owned by others than the author(s) must be honored. Abstracting with credit is permitted. To copy otherwise, or republish, to post on servers or to redistribute to lists, requires prior specific permission and/or a fee. Request permissions from permissions@acm.org.

© 2019 Copyright held by the owner/author(s). Publication rights licensed to ACM. 0730-0301/2019/7-ART116 \$15.00
<https://doi.org/10.1145/3306346.3322937>

1 INTRODUCTION

Conventional 3D imaging systems based on the time-of-flight principle measure the time it takes a light pulse to travel along a direct path from a source, to a visible object, and back to a sensor. Non-line-of-sight (NLOS) imaging, on the other hand, uses multi-bounce light

paths to indirectly measure the 3D shape and visual appearance of hidden objects [Kirmani et al. 2009; Velten et al. 2012] by turning visible surfaces into diffuse reflectors (*cf.* Fig. 1). The NLOS problem is of fundamental importance to many fields (e.g., medical imaging, robotic vision, remote sensing), as the ability to “see” objects hidden from direct line-of-sight has far reaching implications. For instance, NLOS imaging techniques could provide autonomous vehicles a way to see hidden obstacles and navigate around them safely.

Much progress has been made in the emerging field of NLOS imaging (as discussed in Sec. 2), yet significant challenges lie ahead to make this ability practical. First, NLOS light transport models are usually very restrictive, with assumptions that the visible surface is a plane or that hidden objects are Lambertian (diffuse) or retroreflective. Second, the large-scale inverse problems associated with NLOS imaging have traditionally been computationally slow and memory intensive, severely limiting the size of hidden volumes that can be processed. Third, NLOS imaging tends to be a highly light-deficient process. For this reason, the sizes of experimentally captured hidden scenes have been small and retroreflective reflectance properties have been exploited to keep acquisition times reasonable.

In this work, we address these challenges with a new wave-based method, called frequency-wavenumber (or $f-k$) migration, that solves the NLOS problem in closed form. The runtime and memory requirements of our method are orders of magnitude lower than traditional NLOS reconstruction methods such as filtered backprojection (FBP) [Velten et al. 2012], and match the computational performance of the recently proposed light-cone transform (LCT) [O’Toole et al. 2018a], which has been shown to operate at real-time rates using an efficient GPU implementation [O’Toole et al. 2018b]. Yet, the LCT is fundamentally limited in the types of light transport effects it can model adequately. This is primarily due to its geometric optics nature, which only accounts for Lambertian and retroreflective objects, and it has also been restricted to planar scanning surfaces and confocal measurements. $f-k$ migration alleviates these shortcomings while improving robustness to complex scene reflectances and providing superior NLOS reconstruction quality compared to other inverse methods in most cases.

Originally proposed by Stolt [1978] for the application of seismic imaging and later adopted in other domains including synthetic aperture radar (SAR) [Cafforio et al. 1991], $f-k$ migration is the fastest known wave migration method [Margrave and Lamoureux 2018]. We explore the connection between these techniques and the NLOS imaging problem and, more importantly, show how NLOS reconstruction can benefit from algorithmic advances in these fields.

The key contributions of this work include the following:

- We introduce $f-k$ migration to the problem of NLOS imaging and explore the connection between this problem and related challenges in seismic imaging and other fields.
- We demonstrate that $f-k$ migration achieves higher-quality results than other NLOS algorithms, is robust to scenes with complex reflectance properties, and handles non-planar sampling surfaces, as well as confocal and non-confocal scanning approaches.
- We design and build a high-power confocal NLOS system capable of scanning room-sized NLOS scenes with complex reflectance properties and interactive operation “in the wild”.

Table 1. Comparison of NLOS reconstruction algorithms given a $N \times N \times N$ spatio-temporal measurement volume. The FBP method is flexible in being able to handle arbitrary sampling surfaces and scanning schemes, but it is slow and usually leads to low-quality reconstructions. The LCT is fast and accurate, but the method has been constrained by confocal sampling schemes, it has not been demonstrated for non-planar sampling surfaces, and the achieved quality degrades for non-Lambertian objects. The proposed $f-k$ migration algorithm is fast, robust to non-Lambertian reflectance properties, and produces high-quality reconstructions for non-planar sampling surfaces.

	FBP	LCT	$f-k$ mig.
Runtime	$O(N^5)$	$O(N^3 \log N)$	$O(N^3 \log N)$
Memory	$O(N^3)$	$O(N^3)$	$O(N^3)$
Quality	low	medium-high	high
Non-planar surfaces	yes	no	yes
Non-confocal scanning	yes	no	yes
Non-Lambertian objects	no	no	yes

2 RELATED WORK

The foundation of our approach to NLOS imaging spans several fields. We devote this section to reviewing works on optical NLOS imaging, followed by a short overview of techniques used in related fields, including seismic imaging and SAR.

2.1 Optical NLOS Imaging

NLOS imaging, also referred to as “imaging around corners,” is a topic that has received significant attention since being introduced by Kirmani *et al.* [2009]. The idea involves probing a visible wall with an ultrafast laser and detector, and it was later demonstrated in practice with a femtosecond laser and a streak camera [Velten et al. 2012]. The so-called *transient* measurements [Gkioulekas et al. 2015; Lindell et al. 2018; O’Toole et al. 2017; Velten et al. 2013] used in NLOS imaging capture the contribution and travel time of light propagating from one point on a wall, to points in the hidden scene, and back to another point on the wall. Although the ability to image objects hidden from sight is an impressive feat, this initial work also raised many important questions on ways to improve the acquisition and reconstruction procedures.

Due to the expense of femtosecond lasers and streak cameras, some researchers have since opted to use other sensing technologies, including photonic mixer devices (PMDs) used in time-of-flight cameras [Heide et al. 2014] or even regular camera sensors [Klein et al. 2016; Saunders et al. 2019]. However, many have embraced the use of single-photon avalanche diodes (SPADs) for NLOS imaging [Buttafava et al. 2015; O’Toole et al. 2018a; Xu et al. 2018], which are sensors capable of detecting the arrival time of individual photons with a temporal precision on the order of tens of picoseconds. These sensors are relatively versatile, enabling NLOS imaging at long distances, under ambient lighting, or at fast rates [Chan et al. 2017; O’Toole et al. 2018b]. Our solution also makes use of a SPAD sensor paired with a picosecond laser. We refer readers to Altmann *et al.* [2018] for a comprehensive review of SPADs and their applications.

Computationally solving the NLOS reconstruction problem is a major challenge. FBP involves a delay-and-sum operation on transient signals, followed by a Laplacian filter [Velten et al. 2012]. While the results of FBP are promising, the method has several

limitations: the algorithm (1) only gives an approximation of shape and reflectance since it relies on a heuristic filter, (2) makes several restrictive assumptions on light transport (e.g., assumes objects reflect light diffusely, and ignores both occlusions and multi-bounce light transport within the hidden volume) and (3) is very slow.

As a result, a variety of solutions have been proposed, including those that reduce NLOS imaging to a simpler tracking problem [Gariepy et al. 2016], use a parametric planar model to represent the hidden scene [Pediredla et al. 2017a], estimate shape from only the first-returning photons [Tsai et al. 2017], provide a more accurate model for light transport at the cost of higher computational complexity [Heide et al. 2019; Iseringhausen and Hullin 2018], or reconstruct a surface representation of a hidden object by analyzing the geometry of specular paths or by solving an inverse rendering problem [Tsai et al. 2019; Xin et al. 2019]. Others refined the existing NLOS problem statement of Velten et al. [2012] with methods that improve quality with iterative solvers [Gupta et al. 2012; La Manna et al. 2018] or increase computational performance with a fast GPU implementation of FBP [Arellano et al. 2017].

There are also a variety of passive approaches to NLOS imaging [Baradad et al. 2018; Boger-Lombard and Katz 2018; Bouman et al. 2017; Saunders et al. 2019; Thrampoulidis et al. 2018; Torralba and Freeman 2012] or those that rely on laser speckle and the memory effect [Bertolotti et al. 2012; Katz et al. 2014; Smith et al. 2018]. However, these methods provide limited information about the hidden scene, make strong assumptions on light transport (e.g., the presence of occluders), or are limited to microscopic settings.

Other work explores NLOS imaging for varying reflectance properties or surface orientations of the hidden object and visible wall. For example, by illuminating and imaging different parts of the wall, the reflectance properties of a hidden patch with a known spatial location can be determined [Naik et al. 2011]. Alternatively, array signal processing techniques can be related to NLOS imaging to understand how different reflectances of the wall affect resolution bounds [Kadambi et al. 2016]. Other work analyzes how surface orientation affects NLOS feature visibility [Liu et al. 2019] and proposes techniques to bound localization and photometric error [Pediredla et al. 2017b].

With respect to all prior works on optical NLOS imaging, our f - k migration method is most similar to the recent work based on the LCT [O’Toole et al. 2018a] in terms of the low computational complexity and memory requirements (see Table 1). However, the LCT assumes diffuse or retroreflective reflectance and was only shown to work for *confocal* measurements, i.e., transients captured by illuminating and imaging the same point on the wall as shown in Fig. 2. Our method also draws inspiration from wave-based models, an idea briefly discussed in the context of NLOS imaging by Reza et al. [2018a] and explored in more detail in concurrent arXiv works [Liu et al. 2018; Reza et al. 2018b]. However, these works on NLOS imaging use a standard backprojection algorithm which is several orders of magnitude slower than our proposed approach, as detailed in Table 1.

2.2 Seismic, Acoustic, and other Wave-based Imaging

Seismic imaging involves detecting geological interfaces below the earth’s surface [Margrave and Lamoureux 2018], with applications

in oil and gas exploration. An explosion or seismic vibrator generates seismic waves that propagate through the earth, and geophones measure the response at different points on the earth’s surface. Governed by the wave equation, seismic migration is the process of computing the complex subsurface geology that gives rise to the waves detected at the surface, which is mathematically similar to light transport in optical NLOS imaging.

Stolt [1978] introduced frequency-wavenumber migration, commonly referred to as f - k migration, to solve the seismic imaging problem. This algorithm remains the fastest known migration method since its invention, and provides an exact analytical solution for the corresponding wave-based model. It assumes that seismic waves travel at a constant velocity, which unfortunately is generally not the case in seismology (though extensions to f - k migration exist that handle variable wave velocities [Stolt 1978]). Since seismic waves share the same nature as sound waves and even radio waves, f - k migration has also found applications in synthetic aperture sonar (SAS) [Callow 2003; Sheriff 1992], ultrasound imaging [Garcia et al. 2013], and synthetic aperture radar [Cafforio et al. 1991].¹

The propagation of seismic waves also shares many similarities to light transport at visible or near-visible wavelengths, where light waves do generally travel at a constant velocity in free space and are also governed by the wave equation. This connection is exemplified by the proposed use of the LCT method for acoustic NLOS imaging [Lindell et al. 2019], and the existence of an acoustic processing technique analogous to LCT [Norton 1980]. While similarities do exist between mechanical and optical waves, there are also distinct differences in the measurements that require careful treatment, which we address by adapting f - k migration to solve the optical NLOS problem.

Note that longer electromagnetic waves can also pass through walls, rather than scatter off walls. A large body of works therefore exploit this property to perform through-the-wall NLOS imaging using wifi signals [Adib et al. 2015; Adib and Katabi 2013; Zhao et al. 2018] or terahertz radiation [Redo-Sanchez et al. 2016].

3 CONFOCAL NLOS IMAGING USING f - k MIGRATION

The wave equation describes the propagation of electromagnetic radiation (*i.e.*, light). In this section, we show how to express the confocal NLOS image formation model with the wave equation, interpret the NLOS reconstruction problem as a boundary value problem, and introduce the f - k migration technique as a fast closed-form analytical solution to the NLOS reconstruction problem.

3.1 The Wave Equation for NLOS Imaging

Solutions to the time-dependent wave equation accurately model light propagation, including reflections, scattering, and other complex light transport effects. We express the solution as a complex-valued scalar wave field $\Psi(x, y, z, t)$ representing the electromagnetic radiation at every point in space x, y, z and time t .

¹Cafforio [1991] referred to f - k migration as ω - k migration, due to the relationship between frequency f and angular frequency $\omega = 2\pi f$ used in the migration algorithm. The term ω - k migration or range migration algorithm (RMA) is now commonly used in the radar community for historical reasons.

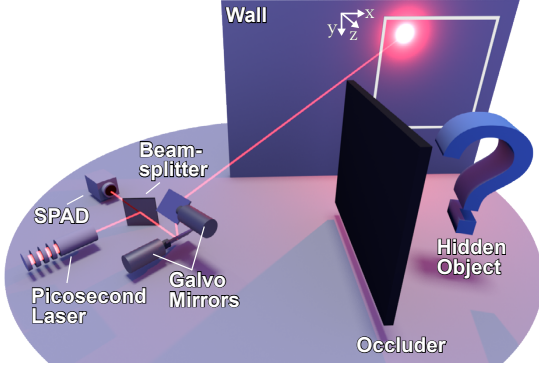


Fig. 2. Illustration of a confocal NLOS system. In this setup, a pulsed picosecond laser sends light to a spot on a visible wall, and a single-photon avalanche diode (SPAD) captures time-varying measurements of the light reflected back in response. Both the laser and SPAD illuminate and image light at the same spot on the wall and operate in a *confocal* configuration. By controlling the angle of the galvo mirrors, the system scans different points on the wall and probes the indirect light reflecting off of the hidden object.

In free space, the wave equation constrains the propagation of Ψ in space and time according to

$$\left(\nabla^2 - \frac{1}{v^2} \frac{\partial^2}{\partial t^2} \right) \Psi = \nabla^2 \Psi - \frac{1}{v^2} \frac{\partial^2 \Psi}{\partial t^2} = 0, \quad (1)$$

where the Laplacian operator $\nabla^2 = \nabla \cdot \nabla = \frac{\partial^2}{\partial x^2} + \frac{\partial^2}{\partial y^2} + \frac{\partial^2}{\partial z^2}$ is defined over the spatial dimensions and the speed of light in the medium is usually defined as $v \approx 3 \cdot 10^8$.

In NLOS imaging, measurements are recorded using an ultrafast detector and a pulsed laser to probe the time-resolved light transport on a visible surface. For simplicity, assume that this surface is planar and located at $z = 0$ for the moment (see Fig. 2). Therefore, we can directly access certain properties of $\Psi(x, y, z = 0, t)$ with the imaging system. Following O'Toole *et al.* [2018a], we interpret the hidden scene as a 3D volume where each point (or voxel, in the discrete case) emits a spherical wave at $t = 0$. Unfortunately, we cannot directly record this scene, so we have to estimate it from the measurements. This is a boundary value problem that requires us to *migrate* the field from one boundary condition (*i.e.*, $z = 0$) to another (*i.e.*, $t = 0$):

$$\Psi(x, y, z = 0, t) \quad \Rightarrow \quad \Psi(x, y, z, t = 0). \quad (2)$$

Note that this interpretation is only correct if the time-resolved measurements are recorded with a confocal imaging system, where one illuminates 2D points on the visible surface while acquiring time-resolved measurements at the same points (see Fig. 2). With this acquisition setup, light propagates to the hidden scene only along very specific paths: from an illuminated point on the visible surface to some hidden point, and back to the same point on the surface. Eqn. (1) models these constraints by setting v to half the speed of light, *i.e.*, $v = \frac{c}{2}$. Coincidentally, this same propagation model is referred to as the “exploding reflector model” in seismology [Margrave and Lamoureux 2018].

With this image formation model, we make the following assumptions: (i) similar to most other NLOS approaches, partial occlusions within hidden scene parts are ignored and (ii) light transport is only modeled from the visible surface to the hidden scene and back (*i.e.*, no multi-bounce transport within the hidden volume). However, no assumptions are explicitly made with respect to the reflectance properties of the hidden objects. Finally, the wave equation models the inverse distance falloff $\frac{1}{r}$ when light propagates from the object to the wall; however, this ignores the falloff due to light propagating in the opposite direction. We therefore account for this in a pre-processing step by multiplying the measured time-varying field by t , where time t is proportional to distance travelled r .

3.2 $f-k$ Migration for NLOS Reconstruction

Many numerical methods exist to compute solutions to the wave equation given some initial conditions, including finite element and finite difference methods. For homogeneous media, $f-k$ migration is the fastest known method and provides an exact solution. As its name suggests, $f-k$ migration relates the two boundary conditions (cf. Eqn. (2)) in the frequency domain.

To understand this approach, let us express the time-dependent field Ψ as a superposition of plane waves:

$$\Psi(x, y, z, t) = \iiint \Phi(k_x, k_y, k_z) e^{2\pi i (k_x x + k_y y + k_z z - f t)} dk_x dk_y dk_z. \quad (3)$$

Here, $\mathbf{k} = 2\pi \cdot (k_x, k_y, k_z)$ is the wave vector indicating the direction of propagation of the individual plane waves, where $|\mathbf{k}| = 2\pi/\lambda$ for optical wavelength λ . The complex-valued function Φ represents the amplitude and phase of each plane wave at time $t = 0$. The wave vector \mathbf{k} and frequency f are related by the dispersion relation $f = v \sqrt{k_x^2 + k_y^2 + k_z^2}$. An important property of Eqn. (3) is that functions Φ and Ψ are related by a Fourier transform when $t = 0$. Please refer to the supplemental material for a detailed derivation of this expression.

Alternatively, one can express Eqn. (3) as an integral over k_x , k_y , and f . This is done by using the dispersion relation and its Jacobian, $\left| \frac{df}{dk_z} \right| = \frac{v |k_z|}{\sqrt{k_x^2 + k_y^2 + k_z^2}}$, to perform a change of variables

$$\Psi(x, y, z, t) = \iiint \bar{\Phi}(k_x, k_y, f) e^{2\pi i (k_x x + k_y y + k_z z - f t)} dk_x dk_y df \quad (4)$$

where

$$\Phi(k_x, k_y, k_z) = \frac{v |k_z|}{\sqrt{k_x^2 + k_y^2 + k_z^2}} \bar{\Phi}\left(k_x, k_y, v \sqrt{k_x^2 + k_y^2 + k_z^2}\right). \quad (5)$$

This expression for the change of variables represents a weighted 1D interpolation, known as Stolt interpolation (see Margrave and Lamoureux [2018] for a useful overview and derivation in the context of seismology). Once again, when $z = 0$, Eqn. (4) becomes a three-dimensional Fourier transformation.

Equipped with Eqns. (3)-(5), $f-k$ migration takes as input a function $\Psi(x, y, z = 0, t)$ and follows three simple steps to migrate the field back to $\Psi(x, y, z, t = 0)$: a 3D Fourier transform of the measurements, a weighted interpolation of the resulting volume, and an inverse 3D Fourier transform. The measurement volume should also be padded with zeros prior to performing the Fourier transform

operation. Refer to Algorithm 1 for pseudo code describing this algorithm. Similarly derived steps can be used to migrate the field in the opposite direction, from $t = 0$ to $z = 0$.

Algorithm 1 f - k migration for NLOS imaging

```

1: procedure FKMIG( $\tau(x, y, t)$ )
2:   // Pre-process data
3:    $\Psi(x, y, t) = t \cdot \sqrt{\tau(x, y, t)}$ 
4:    $\Psi(x, y, t) = \text{pad\_volume}(\Psi(x, y, t))$ 
5:   // Fast Fourier transform (Eqn. (4))
6:    $\Phi(k_x, k_y, f) = \mathcal{F}_{\{x, y, t\}} \{\Psi(x, y, t)\}$ 
7:   // Stolt interpolation (Eqn. (5))
8:    $\Phi(k_x, k_y, k_z) = \frac{v|k_z|}{\sqrt{k_x^2 + k_y^2 + k_z^2}} \cdot \text{resample}(\Phi(k_x, k_y, f))$ 
9:   // Inverse Fast Fourier transform (Eqn. (3))
10:   $\Psi(x, y, z) = \mathcal{F}_{\{x, y, z\}}^{-1} \{\Phi(k_x, k_y, k_z)\}$ 
11:  // Post-process data
12:   $\Psi(x, y, z) = \text{unpad\_volume}(\Psi(x, y, z))$ 
13:  return  $|\Psi(x, y, z)|^2$ 
14: end procedure
  
```

Assuming the measurement and reconstruction volumes have N elements along each dimension, the method requires $O(N^3 \log N)$ operations due to the 3D Fourier transform operations in Algorithm 1, and $O(N^3)$ memory to store the volumes. Because the algorithm relies on Fourier transform operations and a 1D Stolt interpolation procedure, the method is also highly parallelizable.

3.3 Wave Optics Considerations

f - k migration assumes that the amplitude and phase of the complex field $\Psi(x, y, z = 0, t)$ are known, and measurements are usually captured at spatial scales comparable to the surface geometries that cause scattering. The longer wavelengths of seismic, acoustic, and radio waves facilitate direct measurement of the complex fields at these scales. However, optical scattering interactions, which give rise to surface reflectance properties, occur at far finer scales than our measurements captured with visible wavelengths. Thus when applied to optical NLOS imaging, f - k migration is robust, but not completely invariant, to varying scene reflectance properties.

The highly-oscillatory field at optical wavelengths makes it challenging to measure the phase and amplitude of Ψ directly. Typical NLOS systems measure a transient image $\tau(x, y, t) = |\Psi(x, y, z = 0, t)|^2$, capturing only the intensity of the field. While interferometric techniques [Gkioulekas et al. 2015] could potentially be used to capture the phase information, this would require more complicated optical setups. Iterative phase retrieval algorithms can also be applied, but result in a much slower inverse method.

In practice, we observe that simply omitting the phase at the initial boundary conditions, *i.e.*, by setting $\Psi(x, y, z = 0, t) = \sqrt{\tau(x, y, t)}$, produces high-quality reconstructions without any iterations. Similarly, the output of the f - k migration method should also be squared to obtain the final real-valued volume, $|\Psi(x, y, z, t = 0)|^2$. A similar procedure is used in synthetic aperture sonar; phase information is

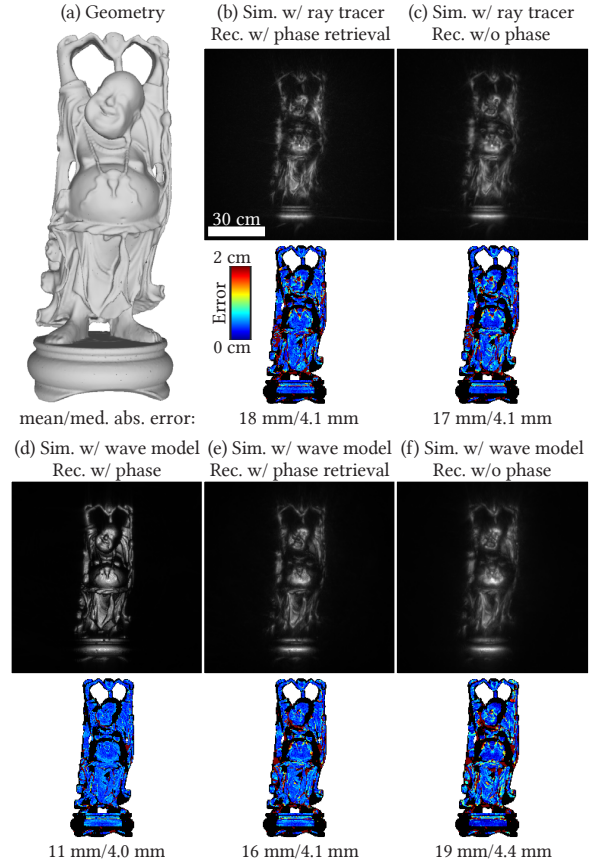


Fig. 3. Evaluation of the effect of phase on f - k migration reconstruction. (a) Geometry of the Happy Buddha. (b-c) We use a ray tracer to simulate measurements for a mirror-like Buddha with the ray tracing procedure described in Sec. 5. Using f - k migration with phase retrieval produces a slightly sharper appearance, but with similar quantitative performance as omitting the phase retrieval step. (d) We also use the wave equation to synthesize complex-valued measurements with phase and amplitude information and apply f - k migration. (e-f) We remove phase information by computing the absolute value of the measurements used in (b) and reconstruct the measurements (e) with phase retrieval or (f) without phase retrieval. While reconstruction quality improves by retrieving phase information, omitting phase produces a similar result with far less computation.

discarded because maintaining phase coherence as measurements are captured is difficult [De Heering 1984; Foo 2004].

In Fig. 3, we evaluate the effect of phase on reconstruction quality by simulating confocal NLOS measurements of a Happy Buddha and performing the reconstruction with f - k migration. The measurements are simulated using a geometric ray tracing technique (described in Sec. 5) or using the wave equation. The ray tracing technique approximates captured NLOS intensity measurements at the correct spatial scales, but lacks phase information. Using the wave equation provides amplitude and phase information, though scattering interactions are simulated at millimeter scales rather than the sub-micron scales of optical wavelengths because of practical computational constraints.

To quantitatively evaluate the accuracy of reconstructed volumes, we generate depth maps by searching for the voxels with maximum intensity along the z -dimension (*i.e.*, in the direction of the wall’s normal), and compare these depth maps to the ground truth geometry. Maximum intensity projection is a common volume visualization technique [Pettersen et al. 2004], which we employ to visualize and evaluate reconstructed geometry.

For Fig. 3(b–c), we use the ray tracing procedure to generate intensity measurements for a specular Buddha, and compare reconstructions using (b) a hybrid input-output iterative phase retrieval algorithm [Fienup 1982] and (c) our heuristic approach of omitting the phase. We run the phase retrieval algorithm for 50 iterations with a step size of 0.01; additional algorithmic details are provided in the supplementary material. While phase retrieval produces a slightly sharper appearance, the methods are quantitatively similar with both having a median absolute error of 4.1 mm.

For Fig. 3(d–f), we simulate both phase and amplitude of the wave field using the wave equation. The volume is reconstructed with $f-k$ migration (d) using the phase information, or (e–f) using the absolute value of the measurements (*i.e.*, omitting the phase) with or without the phase retrieval algorithm. While reconstruction quality is worse when ignoring phase, the features of the Happy Buddha remain clearly discernible. In general, omitting the phase results in reconstruction quality similar to iterative phase retrieval while being much less computationally expensive. All results in the following are reconstructed using this method of omitting the phase, except for an additional comparison on captured data which we provide in the supplementary material.

4 PROTOTYPE SYSTEM

In order to experimentally validate the performance of $f-k$ migration, we built a prototype system which captures confocal NLOS measurements for a variety of scenes at room-sized scales (several meters in each dimension).

4.1 Hardware

Our prototype confocal NLOS system consists of a laser, detector, electronics, and various optics and optomechanical parts used for focusing and scanning. A photo of the prototype is shown in Fig. 4. The system enables faster and higher-resolution scanning with an average laser power roughly 10,000 \times greater than previous confocal NLOS systems [O’Toole et al. 2018a].

A high-power pulsed laser (NKT Photonics OneFive KATANA 05 HP) emits a collimated and linearly polarized beam consisting of 35 ps pulses at a rate of 10 MHz. The average optical power of the emitted laser beam exceeds 1 W at 532 nm. The polarized light passes through a polarized beamsplitter cube (Thorlabs PBS251), and is steered into the scene by a pair of galvanometer mirrors (Thorlabs GVS012) controlled with a National Instruments data acquisition device (NI-DAQ USB-6343). The returning light travels back along the same optical path, is reflected by the polarizing beamsplitter, and is focused by a lens (Canon EF 50 mm f/1.8) onto a detector (see Fig. 4 for illustration of the optical path). Because the wall randomly polarizes light upon reflection, the polarized beamsplitter blocks 50% of the returning light.

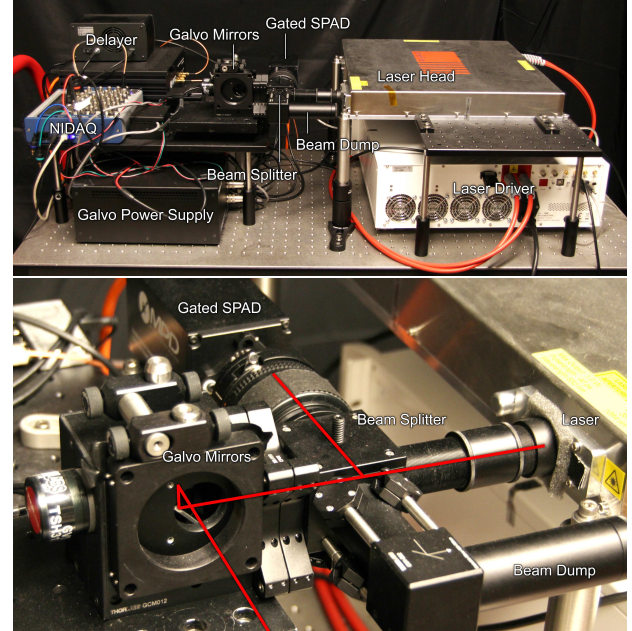


Fig. 4. Prototype confocal NLOS imaging system. A laser emits a short pulse of light that is optically steered by galvo mirrors to scan a scene. Direct and indirect light returns along the same optical path and is measured by a fast-gated single-photon avalanche diode (SPAD).

The detector is a single-pixel fast-gated SPAD (Micro Photon Devices PDM series SPAD) with a $50 \mu\text{m} \times 50 \mu\text{m}$ active image area. A time-correlated single photon counter or TCSPC (PicoQuant PicoHarp 300) takes the signal of the SPAD and laser as input, and outputs a stream of photon timestamps to a computer. In order to avoid the overwhelmingly bright contribution of direct light which returns from the wall, we use the SPAD’s gating capability; this allows us to turn the SPAD on after the direct light arrives and off after capturing the indirect light from the hidden scene (*i.e.*, we use an ultra-fast electronic shutter). The time at which the gate turns on can be variably adjusted by passing the trigger signal from the laser through a delayer unit (PicoQuant MPD Picosecond Delayer) and on to the SPAD. We program the length of the gate in software to be approximately 40 ns, which spans the time over which the indirect light arrives. The temporal resolution of the system, including the laser, SPAD, and TCSPC, is approximately 70 ps.

4.2 Calibration and Scanning Procedure

Calibrating the prototype hardware system requires focusing the lens and aligning the illumination and detection spots. With the laser turned off and ambient lights on, we raster scan 32 \times 32 images of a checkerboard calibration target, and adjust the focus settings to achieve a sharp image. With the laser turned on, we position and orient the beamsplitter cube to align the laser and SPAD. At the highest laser power settings, the direct light from the wall can still overwhelm the SPAD despite its gating capabilities; we therefore intentionally misalign the system in order to illuminate and image two slightly different spots on a wall, reducing the measured intensity of direct light by a factor of approximately 100.

When acquiring measurements, we perform an initial scan of the wall to capture its 3D shape, and use this information to sample measurements across an uniform grid. We also use this information to rapidly adjust the time at which the SPAD gate turns on during scanning, so that measurements are captured just after the direct light from the wall arrives. The vertical scan rate of the system is up to 128 lines per second; this corresponds to scan rates of 4 Hz for 32×32 samples and 2 Hz for 64×64 samples. For long exposures at 512×512 resolution, we scan at a rate of $\frac{1}{15}$ Hz, repeat the scan and sum the measurements over the desired exposure time. Increasing the number of spatial samples improves the lateral resolution of the reconstructed volume up to a bound determined by the system temporal resolution (see supplemental materials for additional information).

4.3 Software

A MATLAB function captures and processes a stream of raw data. This data stream consists of 32-bit data packets for every detected event: 12-bits represent the time-of-flight value of a detected photon measured in increments of 16 ps, 16-bits correspond to a coarse time value measured in microseconds, and 4-bits represent external marker signals. The NI-DAQ passes a VSYNC signal to the TCSPC, injecting marker signals into the data stream that indicate the start of every new frame. The MATLAB function converts the data stream into a measurement volume as follows: for every event in the data stream, the function determines the (x, y) scanning position using the coarse time elapsed since the start of the frame, sets the value t to the corresponding time-of-flight value relative to the direct component that appears at $t = 0$, and increments the value of voxel (x, y, t) within the measurement volume.

The data are processed on a computer with 256 GB of memory and two Intel Xeon E5-2690 v4 CPUs running at 2.60 GHz. With this hardware, our unoptimized MATLAB implementations of $f-k$ migration and the LCT take approximately 80 s and 25 s, respectively for a volume of 512^3 samples. We attribute the difference in reconstruction time to the inefficient implementation of the Stolt interpolation step, which relies on MATLAB's *interp* function. In comparison, FBP requires over 10 hours of compute time for the same volume. A real-time (> 60 reconstructions per second) GPU-based implementation of the LCT was recently demonstrated [O'Toole et al. 2018b], and similar reconstruction speeds could be attained with $f-k$ migration. All captured datasets and reconstruction software are publicly available².

5 RESULTS

Quantitative Evaluation. We quantitatively evaluate $f-k$ migration and LCT through simulations in the following. The scene contains either a specular or diffuse Stanford bunny contained within a $1\text{ m} \times 1\text{ m} \times 1\text{ m}$ hidden volume. Simulated data is processed at a spatial resolution of 256×256 and a temporal resolution of 1024. Each temporal bin spans 16 ps.

Generating simulated confocal measurements of a specular scene is a challenging rendering problem (discussed in Jakob and

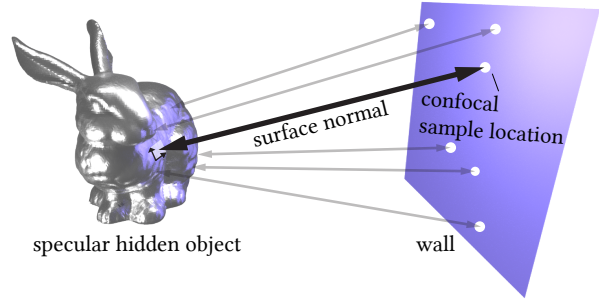


Fig. 5. Illustration of confocal ray tracing procedure for a specular hidden object. Confocal NLOS measurements of a specular hidden object capture light paths which travel from the wall to the hidden object and return to the same position on the wall. We simulate these measurements by randomly sampling the surface of the hidden object, generating a ray whose direction corresponds to the sampled surface normal, intersecting the ray with the wall, and calculating its radiometric contribution and path length.

Marschner [2012]) which requires finding paths that begin at the wall, reflect off of a specular object, and return to the *same* point on the wall. With standard ray tracers, these paths are only found when the sampled random outgoing ray direction from the wall exactly matches the object surface normal at the point of intersection. Since the corresponding subset of paths has measure zero (*i.e.*, they are sampled with zero probability), recent transient renderers [Jarabo et al. 2014, 2017, 2015; Marco et al. 2019] do not sample these troublesome light paths efficiently. We therefore simulate the measurements using a custom ray tracing procedure.

Our custom procedure is illustrated in Fig. 5 and consists of (1) choosing a random 3D point on the hidden object, (2) generating a ray with a direction that matches the corresponding surface normal, (3) intersecting this ray with the wall (if visible), and (4) calculating the radiometric contribution and path length of the corresponding confocal light path. This procedure is limited to capturing 3-bounce specular paths, which contribute the majority of the signal; computing higher-order specular paths is highly non-trivial. We also use this procedure to generate the simulated measurements in Fig. 3 in addition to those in Fig. 6.

Reconstruction of a specular Stanford bunny from simulated transients is shown in Fig. 6. Because the image formation model for LCT strictly assumes diffuse reflectance, artifacts appear in the reconstruction in the form of streaks surrounding the object. We observe that $f-k$ migration produces higher-quality reconstructions for specular objects, since $f-k$ migration makes no explicit assumptions on the reflectance properties of the hidden object. $f-k$ migration outperforms LCT by a factor of $3.5\times$ in terms of mean absolute error, and $1.8\times$ in terms of median absolute error which we calculate using the same procedure as for Fig. 3.

In Fig. 7, we reconstruct the shape and albedo of the bunny from diffuse measurements. In this case, the simulated confocal measurements are provided by O'Toole et al. [2018a], which were rendered through a modified version of PBRT [Pharr et al. 2016]. Despite visual differences in the reconstructed volume, the depth map recovered by $f-k$ migration and LCT are equally accurate in terms of mean absolute error and median absolute error.

²Code and datasets available at <https://github.com/computational-imaging/nlos-fk/> and <http://www.computationalimaging.org/publications/nlos-fk/>

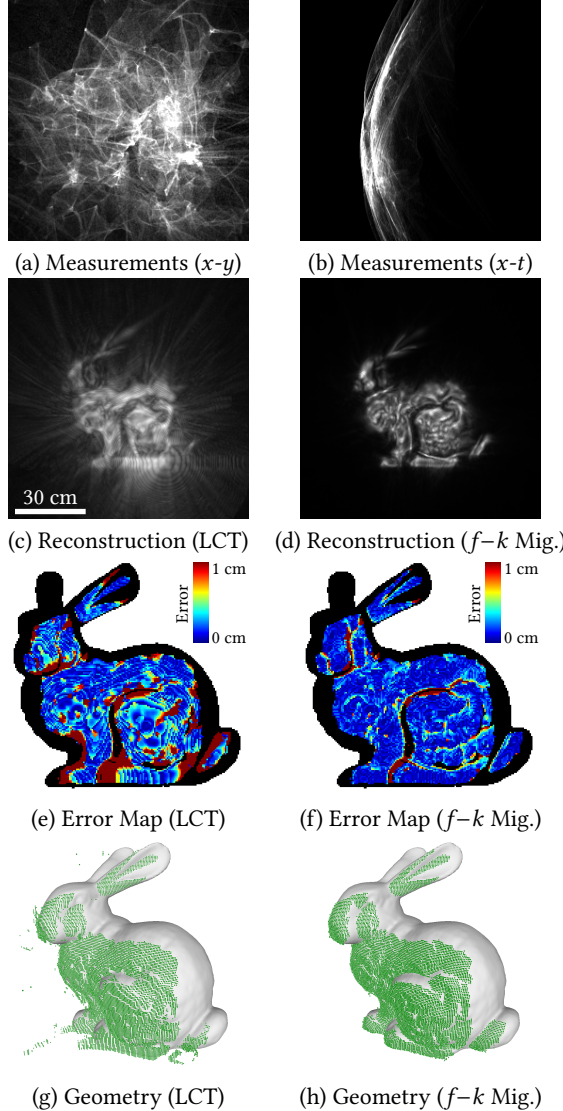


Fig. 6. Comparison of $f-k$ migration and LCT for a specular bunny. **(a-b)** Measurements of the specular bunny scene, visualized as 2D images using a sum-projection. The complex geometry and specular nature of the bunny causes caustics to appear on the wall in (a). **(c-d)** Reconstructed view of the bunny, rendered by taking the maximum intensity projection of the volume along the z -dimension. **(e-f)** Difference in geometry along depth axis. Due to the specular nature of this scene, certain regions on the bunny do not contribute any light to the $1\text{ m} \times 1\text{ m}$ area on the wall; these regions are shown in black and cannot be reconstructed reliably since no signal is present. The mean absolute error of the remaining points is 2.4 mm for $f-k$ migration and 8.4 mm for LCT. Similarly, the median absolute error is 1.3 mm for $f-k$ migration and 2.4 mm for LCT. **(g-h)** Point cloud overlaid to ground truth geometry of bunny.

Indoor Reconstructions. We evaluate $f-k$ migration with our prototype hardware system for a variety of indoor scenes, including a glossy dragon, a diffuse statue, a disco ball, and a hidden room.

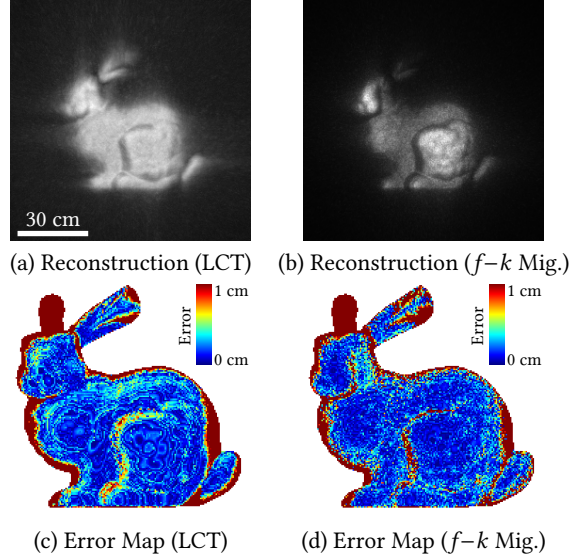


Fig. 7. Comparison of $f-k$ migration and LCT for a diffuse bunny. **(a-b)** Reconstructed view of the bunny by a maximum intensity projection along the z -dimension. **(c-d)** Difference in recovered geometry along depth axis. The mean absolute error of the remaining points is 1.4 cm for $f-k$ migration and 1.3 cm for LCT. Similarly, the median absolute error is 2.1 mm for $f-k$ migration and 2.2 mm for LCT. Note that, unlike Fig. 6, all visible points on the bunny contribute light to the wall; we therefore evaluate reconstruction performance across the entire depth map of the bunny.

The measurements shown in Fig. 8 were captured by scanning a 512×512 grid of points across a $2\text{ m} \times 2\text{ m}$ area on the wall with a total exposure time of 10 min ; longer exposures are shown in the supplemental materials. All three objects shown in this figure have different reflectance properties, ranging from diffuse to specular. Both the reconstruction of $f-k$ migration and LCT tend to be similar for diffuse and glossy objects, though $f-k$ migration generally appears less sensitive to noise present within the measurements. In comparison, FBP tends to perform poorly when measurements contain a large amount of noise. With respect to the disco ball example, $f-k$ migration provides a reasonable reconstruction of the disco ball’s faceted spherical surface, whereas both FBP and LCT suffer from numerous streak-like artifacts. Note that the backprojection step in FBP is exceedingly slow, requiring several hours of compute time; we therefore rely on LCT to quickly perform the backprojection step and apply the Laplacian of a Gaussian filter on the result.

The teaser shown in Fig. 1 consists of a hidden scene containing a variety of objects, including all three objects shown in Fig. 8. This particular scene was captured using a 180 min exposure to show the best reconstruction performance for all three reconstruction methods. Note that $f-k$ migration produces a reconstruction with the fewest visual artifacts due to its relative robustness to the variety of complex reflectances present in the scene. Even though the diffuse statue appears overall dimmer for $f-k$ migration compared to FBP and LCT, $f-k$ migration still reconstructs the features of this statue with high fidelity.

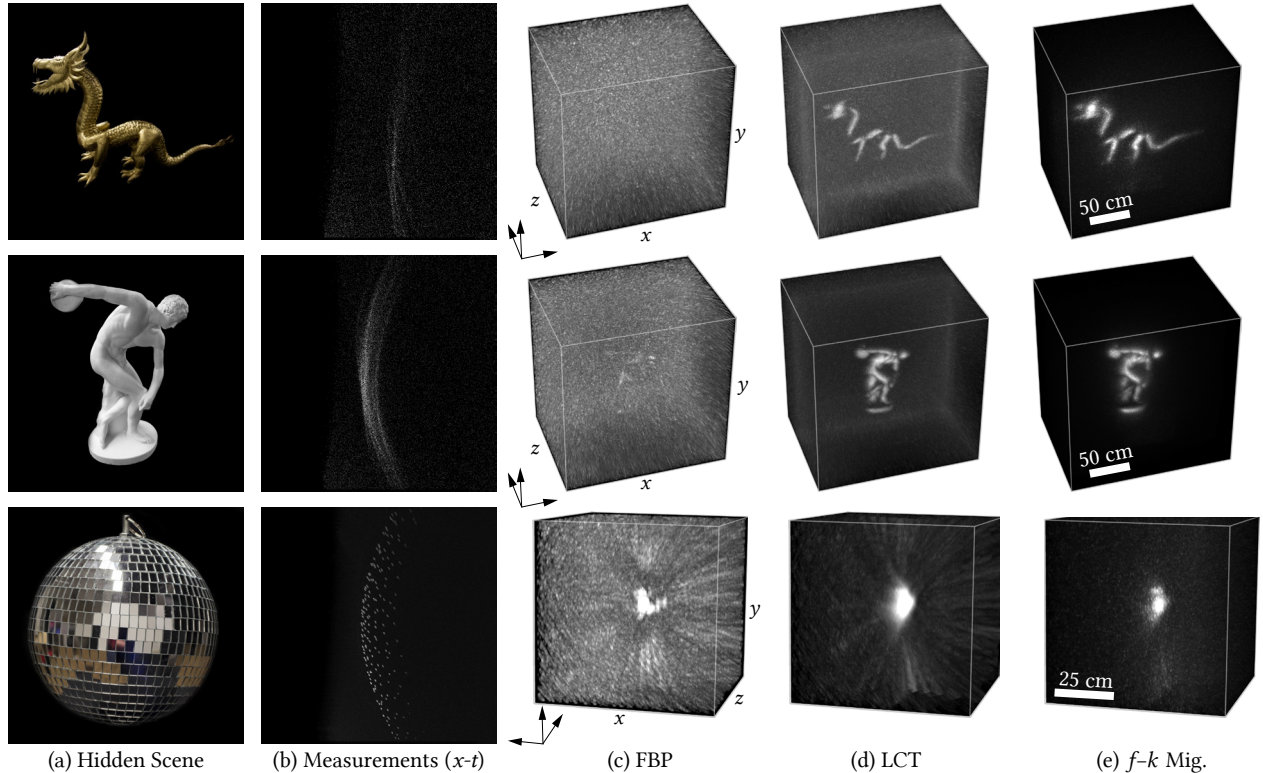


Fig. 8. Comparison of reconstructions from measurements with a 10 min exposure. (a) Photographs of three hidden scenes, including a glossy dragon, a diffuse statue, and a disco ball. (b) $x-t$ slices of the measurement volume for the top two rows (t -axis along the horizontal), and an $x-t$ max-projection for the disco ball measurements (done to better highlight the specular reflections). The prototype system captured measurements over a $2\text{ m} \times 2\text{ m}$ planar wall. (c-e) The reconstruction methods include the (c) FBP, (d) LCT, and (e) our proposed $f-k$ migration method. The reconstructed volumes represent a $2\text{ m} \times 2\text{ m} \times 1.5\text{ m}$ volume of space. Because the disco ball is relatively small, we crop the reconstructed volume to better visualize reconstruction quality.

Sensitivity to Noise. To evaluate the reconstruction methods with respect to noise, we perform reconstructions on measurements of a bike captured over different exposure times in Fig. 9. Please refer to the supplemental materials for more reconstruction times. The shape of the bike is discernible after 180 min for all three methods. However, the FBP reconstruction result is noisier than both $f-k$ migration and LCT, and the LCT results appears to be blurrier than both $f-k$ migration and FBP. $f-k$ migration produces high-fidelity reconstructions while also being robust to noise. With a 10 min exposure, the relative reconstruction quality of $f-k$ migration and LCT remains the same, but the reconstruction quality of FBP degrades appreciably due to its sensitivity to noise.

Also note that past methods such as FBP and LCT require some parameter tuning, especially in the presence of noise. For example, LCT makes use of a user-defined parameter to control its tolerance to noise. $f-k$ migration, on the other hand, has no tunable parameters, and works by simply redistributing frequency coefficients.

NLOS Imaging “In The Wild”. We demonstrate the ability to perform NLOS imaging off of a building under indirect ambient sunlight in Fig. 10. The scene contains the diffuse statue, a table covered by a tablecloth, and a potted plant on top of the table. The measurements were acquired over a 50 min period during twilight between 5:11-6:01 PM on Jan. 4, 2019 under partly sunny conditions. Note

that the visible wall has non-uniform albedo; we choose to not explicitly account for the wall’s varying albedo in our reconstruction procedure, highlighting the robustness of $f-k$ migration in practice.

Dynamic Scene Capture. Our prototype NLOS system can also capture dynamic scenes by scanning walls quickly. In Fig. 11, we capture the shape and position of a person at 4 Hz by sampling a 32×32 grid on the wall. To address the limited signal at such short exposure times, the person is wearing retroreflective clothing that greatly increases the indirect signal detected at the wall. Despite being lower resolution than our long exposure examples, the reconstructions clearly show the person’s position and pose. The reconstruction time for $f-k$ migration is 1.2 s per frame. Please refer to the supplemental video to view the reconstruction.

6 EXTENSIONS TO $f-k$ MIGRATION

In this section, we discuss extensions to the proposed algorithm that allow it to be applied to non-confocally scanned data and to work with non-planar sampling surfaces.

6.1 Processing Non-confocal Measurements

FFT-based methods, including $f-k$ migration and LCT, are fast but limited to processing confocal measurements. However, capturing confocal measurements can be hard, since the measurements include an overwhelming contribution of direct light when illuminating and

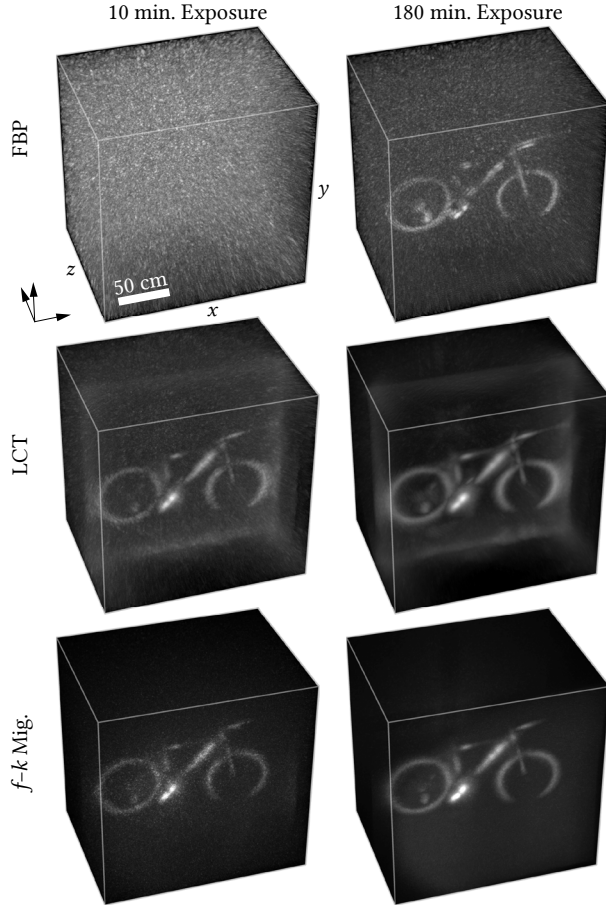


Fig. 9. Comparisons of reconstruction methods with measurements of bike captured at exposure settings of 10 min and 180 min. (**Row 1**) FBP tends to amplify noise within the measurements, and greatly improves with longer exposures. (**Row 2**) LCT is relatively robust to noise with the exception of some border artifacts, but produces the bluriest results in this scene, possibly due to specular reflectance function of the bike's metal frame. (**Row 3**) $f-k$ migration is robust to noise and also produces high-quality results. Refer to the supplemental materials for a picture of the bike.

imaging the same spot on the wall, as mentioned in Sec. 4. Similar physical constraints exist in both seismology and SAR that prevent the co-location of source and detector (e.g., due to constraints on the physical proximity of source and detector in seismology, or caused by the fast motion of satellites in SAR).

Here, we introduce a simple pre-processing step to convert non-confocal measurements to confocal measurements. This correction procedure is based on Normal Moveout Correction [Yilmaz 2001] used in the seismic imaging community, and discussed in Lindell *et al.* [2019] in the context of acoustic NLOS imaging. The approach is to approximate the measurements as though confocally sampled at a common midpoint location of the non-confocal source and detector.

Consider the NLOS imaging scenario in which a sensor images a point (x_c, y_c) , a pulsed laser illuminates a point (x_ℓ, y_ℓ) on a wall located at $z = 0$, and the hidden volume contains a single scatterer located at $(\frac{x_c+x_\ell}{2}, \frac{y_c+y_\ell}{2}, z_p)$. The non-confocal time of flight t is related to the time of flight t_0 of a confocal measurement position

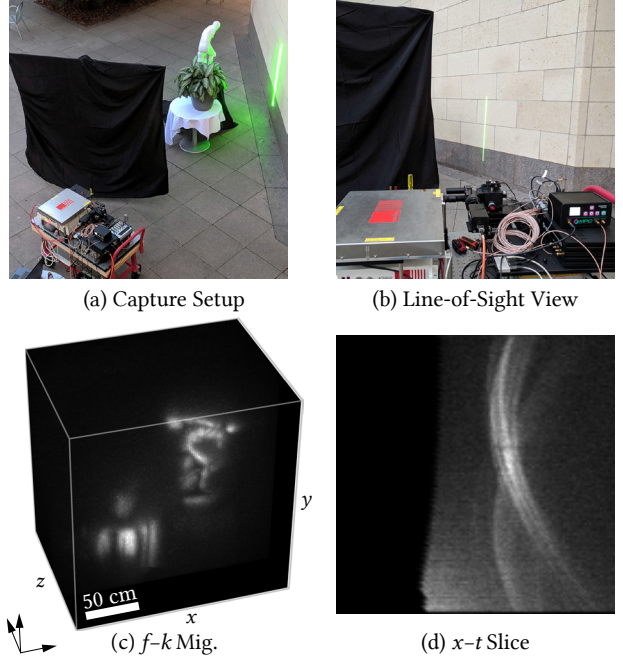


Fig. 10. Outdoor NLOS capture setup and result. (**a**) The NLOS hardware prototype scans a 2×2 m area on the side of a building in front of a scene containing a potted plant on a table and a statue. (**b**) An occluder blocks the line-of-sight view of the hidden scene while the system scans the wall. (**c**) Using $f-k$ migration, the hidden geometry is recovered. (**d**) A $x-t$ slice of the measurements (t -axis along the horizontal) for a 50 min. acquisition period. Note that the dark region on the left-hand side of the image represents the effect of the SPAD's gate, used to remove direct reflections.

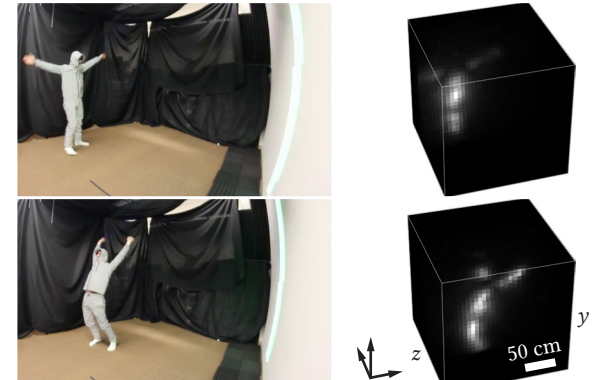


Fig. 11. Reconstruction of a person hidden from view at 4 Hz (*i.e.*, each frame consists of a 0.25 s exposure). To improve signal at short exposures, the person is dressed in a retroreflective suit.

at the midpoint location $(\frac{x_c+x_\ell}{2}, \frac{y_c+y_\ell}{2})$ on the wall by

$$t_0^2 = t^2 - \frac{1}{v^2} \left(|x_c - x_\ell|^2 + |y_c - y_\ell|^2 \right), \quad (6)$$

where $|x_c - x_\ell|$ and $|y_c - y_\ell|$ represent the offset, or distance between the points imaged by the camera and illuminated by the laser. While this expression is only approximate for scatterers whose x and y location deviate from the midpoint, in practice, the error is small

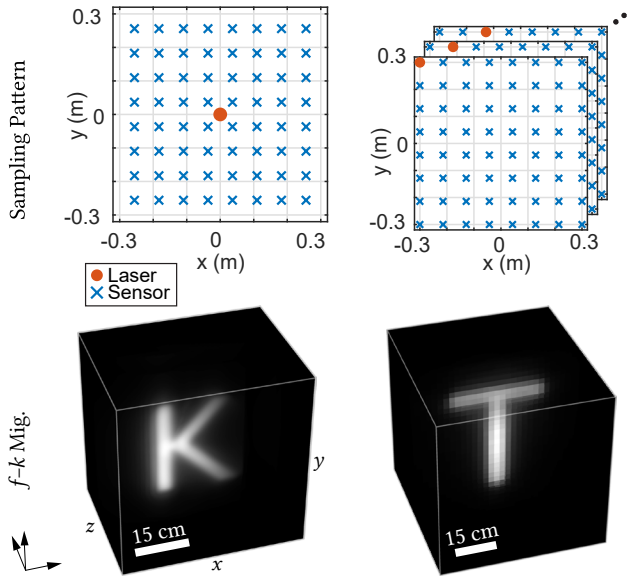


Fig. 12. Reconstructions of non-confocal measurements. Two non-confocal sampling schemes are shown. (**Left column**) The sensor scans across a grid of points on a wall in front of the hidden volume while the laser point is stationary, producing a 2D set of non-confocal transients [Klein et al. 2018]. (**Right column**) A laser and sensor exhaustively scan points across a wall to capture a 4D set of transients.³ After correcting these non-confocal measurements to emulate measurements captured on a confocal grid, $f-k$ migration can be used to reconstruct the hidden volume with greatly reduced computational complexity compared to an algorithm like FBP.

for distances larger than a few tens of centimeters away from the wall and can typically be neglected, especially for NLOS systems with temporal resolution in the tens of picoseconds.

The process to calculate the confocal approximation to non-confocal measurements thus consists of three steps: (i) reparameterize the measurements by their midpoint locations and offsets instead of camera and laser sample locations; (ii) for each midpoint and offset, interpolate the transient measurement using the relationship of Eqn. (6) to estimate the confocal transient at the midpoint; and (iii) average the measurements across the offset dimensions to yield the 3D volume of confocal measurements sampled on the midpoint grid.

Because our prototype system only captures confocal NLOS measurements, we demonstrate this correction step for $f-k$ migration in Fig. 12 on two simulated non-confocal datasets, where the laser is either stationary [Klein et al. 2018] or the laser and detector are exhaustively scanned.³ In the former case, a sensor images 256×256 points on the wall over a $0.512 \text{ m} \times 0.512 \text{ m}$ area, and the laser illuminates a point in the center of the scanned area as illustrated in Fig. 12. The hidden object is placed 0.5 m away from the wall, and the reconstructed volume measures $0.256 \text{ m} \times 0.256 \text{ m} \times 0.2 \text{ m}$ in the x , y , and z dimensions. In the exhaustively scanned case, the laser samples a grid of 16×16 points over a $0.6 \text{ m} \times 0.6 \text{ m}$ area. For each laser position, the sensor observes each point on the same grid. The hidden object, shown in Fig. 12, is located 0.5 m from the wall, and

³ Zaragoza NLOS synthetic dataset by Galindo et al. (accessed on Jan. 8, 2019): http://graphics.unizar.es/nlos_dataset.html.

the reconstructed volume measures $0.6 \text{ m} \times 0.6 \text{ m} \times 0.6 \text{ m}$. While the results of FBP are comparable to those of $f-k$ migration and LCT for these simple scenes (see supplementary information), the computational requirements are drastically reduced using the confocal correction together with $f-k$ migration.

6.2 Processing Non-planar Sampling Surfaces

The $f-k$ migration algorithm reconstructs a hidden volume where $z \geq 0$, and it is assumed that a planar wall was sampled at $z = 0$. This is non-ideal for several reasons, since a large region between the wall and hidden scene is empty space (wasting computational resources) and the wall itself may not always be planar. The former is particularly important to consider in the context of SAR, where an orbiting satellite remotely images the earth's geometry with radio waves from hundreds of kilometers above the surface.

Consider the case of sampling measurements at a constant offset location, $z = \Delta z$, and we desire to extrapolate the value of the field at $z = 0$. As applied to Eqn. (4), this can be expressed as

$$\Psi(x, y, z = 0, t) = \iiint \bar{\Phi}(k_x, k_y, f, z = \Delta z) e^{2\pi i k_z \Delta z} e^{2\pi i (k_x x + k_y y - f t)} dk_x dk_y df \quad (7)$$

Compensating for the constant offset Δz in the position of the wall amounts to multiplying the Fourier transform of the measurements shown in Eqn. (7) by an extrapolation operator $e^{2\pi i k_z \Delta z}$, where $k_z = \sqrt{f^2/v^2 - k_x^2 - k_y^2}$. Intuitively, this operator applies the appropriate phase shifts such that the resulting quantity represents the wave as if measured across a virtual plane at $z = 0$ [Margrave and Lamoureux 2018].

The same extrapolation procedure can be applied to migrate data sampled across a general non-planar surface onto a virtual planar wall at $z = 0$. Let the z -positions of the non-planar surface be parameterized by the function $\Delta z(x, y)$. Then, taking advantage of the linearity of Eqn. (7), the procedure involves three steps: (i) isolate the measurement transient at each spatial location (x, y) and compute its 3D-Fourier transform; (ii) apply the extrapolation operator to shift each transient by $\Delta z(x, y)$; and (iii) linearly combine the resulting spectra of all shifted transients to recover $\bar{\Phi}(k_x, k_y, f, z = 0)$. This pre-processing step can be computationally optimized by processing multiple transients sharing the same offset $\Delta z(x, y)$.

The non-planar sampling procedure is demonstrated with our prototype NLOS system in Fig. 13. We measure two hidden retroreflective objects with our prototype NLOS system, where the scanning surface has non-planar geometry. While methods such as FBP can handle non-planar objects, it remains slow. Applying $f-k$ migration (or LCT) on non-planar measurements produces a poor reconstruction result, due to the mismatch between the data and the image formation model. By extrapolating the measurements to a plane at $z = 0$ in a pre-processing step and applying $f-k$ migration on the result, we achieve a much improved reconstruction of the hidden scene.

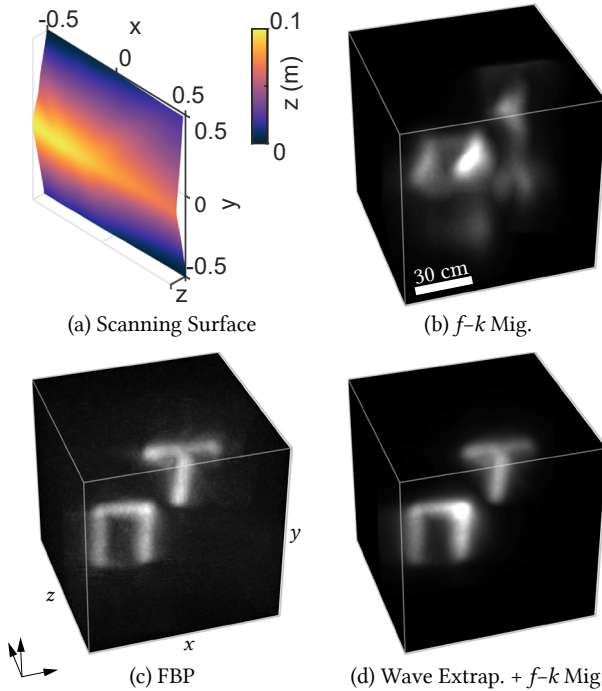


Fig. 13. Non-planar NLOS imaging results. (a) Measurements are captured on a non-planar scanning surface. (b) Without correcting the measurements, $f-k$ migration fails to reconstruct the hidden scene. (c) FBP can account for the non-planar surface intrinsically in the reconstruction, but is less robust to noise and is slow. (d) Applying the wave extrapolation operator to estimate measurements captured on a planar surface and then using $f-k$ migration accurately reconstructs the 3D volume.

7 DISCUSSION

In summary, we propose a wave migration procedure to solve the confocal NLOS reconstruction problem. Compared to other reconstruction methods such as FBP and LCT, $f-k$ migration produces high-quality reconstruction results for scenes containing a variety of reflectance functions (e.g., diffuse, specular), even in the presence of noise. We perform reconstructions on simulated data and experimental data captured with a prototype NLOS system.

Limitations. While $f-k$ migration provides an exact solution to the wave equation, the wave migration model and the standard NLOS image formation based on geometric optics are not equivalent. First, our prototype system and implementation of $f-k$ migration process amplitude measurements, but ignore the effect of phase. This results in reconstruction error, as shown in Fig. 3. Second, the wave field is highly oscillatory; the frequency of visible light may be too high to be accurately modeled with $f-k$ migration at the scales we are working with.

Moreover, while the diffuse and specular reflections are caused by an object's surface geometry, this occurs at microscopic scales. As a result, $f-k$ migration only serves as an approximate solution to the NLOS problem, even though it performs well in comparison to state of the art solutions.

With respect to practical limitations, time-resolved NLOS imaging remains an inherently light deficient problem, because light must

bounce three or more times through the environment to reach the hidden scene. Every scattering event causes a dramatic decrease in the intensity of the returning signal. This is a limitation that applies to all existing time-resolved NLOS methods, including $f-k$ migration.

There are at least three ways to address light efficiency: increasing the brightness of hidden objects (e.g., by scanning retroreflective objects), extending the exposure period, and increasing the available light. However, most objects are not retroreflective, and long exposure periods fail to capture dynamic scenes. The high-power ($>1\text{ W}$) laser in our prototype system is also a safety hazard, requiring protective laser safety glasses and operation by a trained individual to minimize the risk of an eye injury.

Future Work. With respect to improving reconstruction times, the obvious next step is to implement the $f-k$ migration procedure on a GPU. $f-k$ migration is a highly parallelizable procedure and can therefore be significantly accelerated with a GPU implementation. Similar to the real-time implementation of LCT [O'Toole et al. 2018b], we expect a GPU-based $f-k$ migration procedure requires only a few milliseconds of processing time for a sufficiently small reconstruction volume (e.g., 32×32 spatial samples).

Our $f-k$ migration procedure also currently does not take advantage of any image priors, including the known noise characteristics of our SPAD sensor, a non-negativity constraint on albedos, and a spatial sparsity assumption for the scene's hidden geometry. Similar to previously described iterative LCT procedures [O'Toole et al. 2018a], an iterative $f-k$ migration procedure could incorporate these priors to achieve even higher-fidelity NLOS reconstructions.

Conclusion. The ability to image objects hidden from sight has a variety of applications in remote imaging and surveillance. By drawing inspiration and adapting ideas from over 40 years of work since Stolt's original work in seismology [1978], our solution to the NLOS problem provides superior reconstruction results than the current state of the art. We also foresee $f-k$ migration potentially becoming a useful numerical method for migrating optical wave fields in other areas of computer graphics and vision, especially at microscopic scales (e.g., computational microscopy, computer-generated holography).

ACKNOWLEDGMENTS

The authors thank Ioannis Gkioulekas for his helpful feedback. This project was supported by a Stanford Graduate Fellowship, an NSF CAREER Award (IIS 1553333), a Terman Faculty Fellowship, a Sloan Fellowship, by the KAUST Office of Sponsored Research through the Visual Computing Center CCF grant, the DARPA REVEAL program, and the ARO (ECASE-Army Award W911NF-19-1-0120).

REFERENCES

- Fadel Adib, Chen-Yu Hsu, Hongzi Mao, Dina Katabi, and Frédéric Durand. 2015. Capturing the human figure through a wall. *ACM Trans. Graph.* 34, 6 (2015), 219.
- Fadel Adib and Dina Katabi. 2013. See through walls with WiFi!. In *ACM SIGCOMM*.
- Yoann Altmann, Stephen McLaughlin, Miles J. Padgett, Vivek K. Goyal, Alfred O. Hero, and Daniele Faccio. 2018. Quantum-inspired computational imaging. *Science* 361, 6403 (2018).
- Victor Arellano, Diego Gutierrez, and Adrian Jarabo. 2017. Fast back-projection for non-line-of-sight reconstruction. *Optics Express* 25, 10 (2017), 11574–11583.
- Manel Baradad, Vickie Ye, Adam B. Yedidia, Frédéric Durand, William T Freeman, Gregory W Wornell, and Antonio Torralba. 2018. Inferring Light Fields From Shadows. In *Proc. CVPR*.

- Jacopo Bertolotti, Elbert G. van Putten, Christian Blum, Ad Lagendijk, Willem L. Vos, and Allard P. Mosk. 2012. Non-invasive imaging through opaque scattering layers. *Nature* 491, 7423 (2012), 232.
- Jeremy Boger-Lombard and Ori Katz. 2018. Non line-of-sight localization by passive optical time-of-flight. *arXiv preprint arXiv:1808.01000* (2018).
- Katherine L. Bouman, Vickie Ye, Adam B. Yedidia, Frédo Durand, Gregory W Wornell, Antonio Torralba, and William T Freeman. 2017. Turning corners into cameras: Principles and methods. In *Proc. ICCV*.
- Mauro Buttafava, Jessica Zeman, Alberto Tosi, Kevin Eliceiri, and Andreas Velten. 2015. Non-line-of-sight imaging using a time-gated single photon avalanche diode. *Optics Express* 23, 16 (2015), 20997–21011.
- Ciro Cafforio, Claudio Prati, and Fabio Rocca. 1991. SAR data focusing using seismic migration techniques. *IEEE Trans. Aerosp. Electron. Syst.* 27, 2 (1991), 194–207.
- Hayden J. Callow. 2003. *Signal processing for synthetic aperture sonar image enhancement*. Ph.D. Dissertation. University of Canterbury.
- Susan Chan, Ryan E Warburton, Genevieve Gariepy, Jonathan Leach, and Daniele Faccio. 2017. Non-line-of-sight tracking of people at long range. *Optics Express* 25, 9 (2017), 10109–10117.
- Philippe De Heering. 1984. Alternate schemes in synthetic aperture sonar processing. *IEEE J. Ocean. Eng.* 9, 4 (1984), 277–280.
- James R Fienup. 1982. Phase retrieval algorithms: a comparison. *Applied optics* 21, 15 (1982), 2758–2769.
- Kae Yeet Foo. 2004. *Incoherent processing of synthetic aperture sonar*. Ph.D. Dissertation. University of Birmingham.
- Damien Garcia, Louis Le Tarnec, Stéphan Muth, Emmanuel Montagnon, Jonathan Porée, and Guy Cloutier. 2013. Stolt's fk migration for plane wave ultrasound imaging. *IEEE Trans. Ultrason., Ferroelectr., Freq. Control* 60, 9 (2013), 1853–1867.
- Genevieve Gariepy, Francesco Tonolini, Robert Henderson, Jonathan Leach, and Daniele Faccio. 2016. Detection and tracking of moving objects hidden from view. *Nature Photonics* 10, 1 (2016), 23–26.
- Ioannis Gkioulekas, Anat Levin, Frédo Durand, and Todd Zickler. 2015. Micron-scale light transport decomposition using interferometry. *ACM Trans. Graph.* 34, 4 (2015), 37.
- Otkrist Gupta, Thomas Willwacher, Andreas Velten, Ashok Veeraraghavan, and Ramesh Raskar. 2012. Reconstruction of hidden 3D shapes using diffuse reflections. *Optics Express* 20, 17 (2012), 19096–19108.
- Felix Heide, Matthew O'Toole, Kai Zhang, David B. Lindell, Steven Diamond, and Gordon Wetzstein. 2019. Non-line-of-sight imaging with partial occluders and surface normals. *ACM Trans. Graph.* (2019).
- Felix Heide, Lei Xiao, Wolfgang Heidrich, and Matthias B. Hullin. 2014. Diffuse mirrors: 3D reconstruction from diffuse indirect illumination using inexpensive time-of-flight sensors. In *Proc. CVPR*.
- Julian Iseringhausen and Matthias B. Hullin. 2018. Non-line-of-sight reconstruction using efficient transient rendering. *arXiv preprint arXiv:1809.08044* (2018).
- Wenzel Jakob and Steve Marschner. 2012. Manifold exploration: a Markov Chain Monte Carlo technique for rendering scenes with difficult specular transport. *ACM Trans. Graph.* 31, 4 (2012), 58.
- Adrian Jarabo, Julio Marco, Adolfo Muñoz, Raul Buisan, Wojciech Jarosz, and Diego Gutierrez. 2014. A Framework for Transient Rendering. *ACM Trans. Graph.* 33, 6 (2014).
- Adrian Jarabo, Belen Masia, Julio Marco, and Diego Gutierrez. 2017. Recent advances in transient imaging: A computer graphics and vision perspective. *Visual Informatics* 1, 1 (2017), 65–79.
- Adrian Jarabo, Belen Masia, Andreas Velten, Christopher Barsi, Ramesh Raskar, and Diego Gutierrez. 2015. Relativistic effects for time-resolved light transport. In *Computer Graphics Forum*, Vol. 34.
- Achuta Kadambi, Hang Zhao, Boxin Shi, and Ramesh Raskar. 2016. Occluded imaging with time-of-flight sensors. *ACM Trans. Graph.* 35, 2 (2016), 15.
- Ori Katz, Pierre Heidmann, Mathias Fink, and Sylvain Gigan. 2014. Non-invasive single-shot imaging through scattering layers and around corners via speckle correlations. *Nature Photonics* 8, 10 (2014), 784.
- Ahmed Kirmani, Tyler Hutchison, James Davis, and Ramesh Raskar. 2009. Looking around the corner using transient imaging. In *Proc. ICCV*.
- Jonathan Klein, Martin Laurenzis, Dominik L. Michels, and Matthias B. Hullin. 2018. A quantitative platform for non-line-of-sight imaging problems. In *Proc. BMVC*.
- Jonathan Klein, Christoph Peters, Jaime Martín, Martin Laurenzis, and Matthias B. Hullin. 2016. Tracking objects outside the line of sight using 2D intensity images. *Scientific Reports* 6 (2016), 32491.
- Marco La Manna, Fiona Kine, Eric Breitbach, Jonathan Jackson, Talha Sultan, and Andreas Velten. 2018. Error backprojection algorithms for non-line-of-sight imaging. *IEEE Trans. Pattern Anal. Mach. Intell.* (2018).
- David B Lindell, Matthew O'Toole, and Gordon Wetzstein. 2018. Towards transient imaging at interactive rates with single-photon detectors. In *Proc. ICCP*.
- David B. Lindell, Gordon Wetzstein, and Vladlen Koltun. 2019. Acoustic non-line-of-sight imaging. In *Proc. CVPR*.
- Xiaochun Liu, Sebastian Bauer, and Andreas Velten. 2019. Analysis of feature visibility in non-line-of-sight measurements. In *Proc. CVPR*.
- Xiaochun Liu, Ibón Guillén, Marco La Manna, Ji Hyun Nam, Syed Azer Reza, Toan Huu Le, Diego Gutierrez, Adrian Jarabo, and Andreas Velten. 2018. Virtual wave optics for non-line-of-sight imaging. *arXiv preprint arXiv:1810.07535* (2018).
- Julio Marco, Ibón Guillén, Wojciech Jarosz, Diego Gutierrez, and Adrian Jarabo. 2019. Progressive transient photon beams. *Computer Graphics Forum* 38, 1 (2019).
- Gary F. Margrave and Michael P. Lamoureux. 2018. *Numerical Methods of Exploration Seismology: With Algorithms in MATLAB®*. Cambridge University Press.
- Nikhil Naik, Shuang Zhao, Andreas Velten, Ramesh Raskar, and Kavita Bala. 2011. Single view reflectance capture using multiplexed scattering and time-of-flight imaging. 30, 6 (2011), 171.
- Stephen J Norton. 1980. Reconstruction of a reflectivity field from line integrals over circular paths. *The Journal of the Acoustical Society of America* 67, 3 (1980), 853–863.
- Matthew O'Toole, Felix Heide, David B. Lindell, Kai Zang, Steven Diamond, and Gordon Wetzstein. 2017. Reconstructing transient images from single-photon sensors. In *Proc. CVPR*.
- Matthew O'Toole, David B. Lindell, and Gordon Wetzstein. 2018a. Confocal non-line-of-sight imaging based on the light-cone transform. *Nature* 555, 7696 (2018), 338.
- Matthew O'Toole, David B. Lindell, and Gordon Wetzstein. 2018b. Real-time non-line-of-sight imaging. In *ACM SIGGRAPH Emerging Technologies*.
- Adithya Kumar Pedireddla, Mauro Buttafava, Alberto Tosi, Oliver Cossairt, and Ashok Veeraraghavan. 2017a. Reconstructing rooms using photon echoes: A plane based model and reconstruction algorithm for looking around the corner. In *Proc. ICIP*.
- Adithya Kumar Pedireddla, Nathan Matsuda, Oliver Cossairt, and Ashok Veeraraghavan. 2017b. Linear systems approach to identifying performance bounds in indirect imaging. In *Proc. ICASSP*.
- Eric F Pettersen, Thomas D Goddard, Conrad C Huang, Gregory S Couch, Daniel M Greenblatt, Elaine C Meng, and Thomas E Ferrin. 2004. UCSF Chimera—a visualization system for exploratory research and analysis. *Journal of computational chemistry* 25, 13 (2004), 1605–1612.
- Matt Pharr, Wenzel Jakob, and Greg Humphreys. 2016. *Physically based rendering: From theory to implementation*. Morgan Kaufmann.
- Albert Redo-Sanchez, Barmak Heshmat, Alireza Aghasi, Salman Naqvi, Mingjie Zhang, Justin Romberg, and Ramesh Raskar. 2016. Terahertz time-gated spectral imaging for content extraction through layered structures. *Nature communications* 7 (2016), 12665.
- Syed Azer Reza, Marco La Manna, and Andreas Velten. 2018a. Imaging with phasor fields for non-line-of-sight applications. In *Computational Optical Sensing and Imaging*.
- Syed Azer Reza, Marco La Manna, and Andreas Velten. 2018b. A physical light transport model for non-line-of-sight imaging applications. *arXiv preprint arXiv:1802.01823* (2018).
- Charles Saunders, John Murray-Bruce, and Vivek K Goyal. 2019. Computational periscopy with an ordinary digital camera. *Nature* 565, 7740 (2019), 472.
- Robert W. Sheriff. 1992. Synthetic aperture beamforming with automatic phase compensation for high frequency sonars. In *Proc. AUV*.
- Brandon M. Smith, Matthew O'Toole, and Mohit Gupta. 2018. Tracking multiple objects outside the line of sight using speckle imaging. In *Proc. CVPR*.
- Robert H. Stolt. 1978. Migration by Fourier transform. *Geophysics* 43, 1 (1978), 23–48.
- Christos Thrampoulidis, Gal Shulkin, Feihu Xu, William T Freeman, Jeffrey H Shapiro, Antonio Torralba, Franco NC Wong, and Gregory W Wornell. 2018. Exploiting occlusion in non-line-of-sight active imaging. *IEEE Trans. Comput. Imag.* 4, 3 (2018), 419–431.
- Antonio Torralba and William T. Freeman. 2012. Accidental pinhole and pinspeak cameras: Revealing the scene outside the picture. In *Proc. CVPR*.
- Chia-Yin Tsai, Kiriakos N. Kutulakos, Srinivasa G. Narasimhan, and Aswin C. Sankaranarayanan. 2017. The geometry of first-returning photons for non-line-of-sight imaging. In *Proc. CVPR*.
- Chia-Yin Tsai, Aswin Sankaranarayanan, and Ioannis Gkioulekas. 2019. Beyond volumetric albedo—A surface optimization framework for non-line-of-sight imaging. In *Proc. CVPR*.
- Andreas Velten, Thomas Willwacher, Otkrist Gupta, Ashok Veeraraghavan, Moungi G. Bawendi, and Ramesh Raskar. 2012. Recovering three-dimensional shape around a corner using ultrafast time-of-flight imaging. *Nature communications* 3 (2012), 745.
- Andreas Velten, Di Wu, Adrian Jarabo, Belen Masia, Christopher Barsi, Chinmaya Joshi, Everett Lawson, Moungi Bawendi, Diego Gutierrez, and Ramesh Raskar. 2013. Femto-photography: capturing and visualizing the propagation of light. *ACM Trans. Graph.* 32, 4 (2013), 44.
- Shumian Xin, Sotiris Nousias, Kyros Kutulakos, Aswin Sankaranarayanan, Srinivasa Narasimhan, and Ioannis Gkioulekas. 2019. A theory of Fermat paths for non-line-of-sight shape reconstruction. In *Proc. CVPR*.
- Feihu Xu, Gal Shulkin, Christos Thrampoulidis, Jeffrey H Shapiro, Antonio Torralba, Franco NC Wong, and Gregory W Wornell. 2018. Revealing hidden scenes by photon-efficient occlusion-based opportunistic active imaging. *Optics express* 26, 8 (2018), 9945–9962.
- Öz Yilmaz. 2001. *Seismic data analysis: Processing, inversion, and interpretation of seismic data*. Society of Exploration Geophysicists.
- Mingmin Zhao, Tianhong Li, Mohammad Abu Alsheikh, Yonglong Tian, Hang Zhao, Antonio Torralba, and Dina Katabi. 2018. Through-wall human pose estimation using radio signals. In *Proc. CVPR*.